ELSEVIER

Contents lists available at ScienceDirect

# Earth and Planetary Science Letters

www.elsevier.com/locate/epsl



# Diffusive fractionation of K isotopes in molten basalts

Youxue Zhang (张有学)

Department of Earth and Environmental Sciences, the University of Michigan, Ann Arbor, MI 48109, USA



### ARTICLE INFO

Article history:
Received 13 July 2021
Received in revised form 21 December 2021
Accepted 26 January 2022
Available online xxxx
Editor: R. Dasgupta

Keywords:
potassium isotopes
K diffusivity
diffusive isotope fractionation
diffusion mechanism
K-Ar dating
K isotopes in the Moon

#### ABSTRACT

The 41K/39K isotope ratio profiles in diffusion couple experiments have been measured by Secondary Ion Mass Spectrometry (SIMS). One goal of this research is to push the use of SIMS in measuring non-traditional stable isotope ratios. The second, more important goal, is to quantify for the first time diffusive fractionation of K isotopes and its dependence on temperature and different counter-diffusion elements. The data show that the precision in a single day-night session of SIMS measurements can reach 0.2% ( $1\sigma$  hereafter) with effort, and the long-term accuracy without using any isotope ratio standard is about 2.5%. At an initial concentration contrast (ratio of high concentration to low concentration) of about 70 in a diffusion couple, the total <sup>41</sup>K/<sup>39</sup>K fractionation (maximum minus minimum) is about 10%. The  $^{41}$ K/ $^{39}$ K ratio profiles were initially fit by assuming constant effective binary diffusivity (D) of K<sub>2</sub>O, which led to minor misfits and more importantly, to large disagreement between diffusivities based on chemical diffusion and isotope diffusion profiles. It was found that D for K2O varies with its concentration. The profiles were then fit by assuming D for K2O increases exponentially with K2O concentration, which resolved the misfits and disagreements. That is, combining concentration and isotope ratio profiles enables distinguishing subtle concentration-dependent diffusivity. For the SiO2-K2O interdiffusion couples, the empirical diffusive isotope fractionation parameter  $\beta$  increases slightly with temperature from  $0.104 \pm 0.003$  at  $1260\,^{\circ}\text{C}$  to  $0.116 \pm 0.003$  at  $1500\,^{\circ}\text{C}$ . For the MgO-K<sub>2</sub>O interdiffusion couples, excluding an outlier point at 1260 °C,  $\beta$  increases from 0.090  $\pm$  0.005 at 1350 °C to 0.100  $\pm$ 0.003 at 1500 °C. These  $\beta$  values are roughly consistent with a diffusion mechanism of NaKO exchanging with SiO2 in the SiO2-K2O interdiffusion couples, or NaKO exchanging with MgO in the MgO-K2O interdiffusion couples. Applying the obtained  $\beta$  value to model diffusive isotope fractionation in nature, diffusive K isotope fractionation during magma mixing is expected to be large enough to be resolvable by SIMS. When collecting samples for K-Ar or K-Ca dating, it is important to correct for the effect of possible K isotope fractionation by measuring K isotope ratio in the sample. When diffusive and convectivediffusive modeling was applied to evaluate isotope fractionation during volatile loss through diffusion and evaporation, it is found that a loss of 80% potassium would lead to an increase of  $\delta^{41}$ K by 6.3% to 8.9%, more than 10 times greater than the enrichment of  $\delta^{41}$ K in the Moon relative to the Earth. Hence, the depletion of K and the associated enrichment of  $\delta^{41}$ K in the Moon relative to the Earth are unlikely diffusion controlled.

© 2022 Elsevier B.V. All rights reserved.

### 1. Introduction

Stable isotope fractionation during diffusion has applications in the transport and separation of isotopes, and provides insight on the mechanism of diffusion at the molecular and ionic level. In igneous processes, diffusive stable isotope fractionation may occur during mineral growth/dissolution (e.g., Jambon, 1980; Watkins et al., 2017), and magma mixing and interaction (e.g., Chopra et al., 2012; Wu et al., 2018). Such fractionation may be used to probe mineral growth or dissolution rates as well as the cooling rate of

rocks. Another potential application of K stable isotope fractionation is its effect on high-precision dating.

Even though diffusion tends to reduce concentration gradients, interestingly it may lead to significant isotope ratio differences in an initially isotopically homogeneous system but with chemical concentration gradients. In fact, diffusive isotope fractionation can be much larger than equilibrium isotope fractionation, especially at high temperatures (e.g., Richter et al., 2009b). For example, natural  $^{41}\mathrm{K}/^{39}\mathrm{K}$  isotope ratio in volcanic rocks in  $\delta^{41}\mathrm{K}$  notation (to be defined later) ranges from -1.55% (Wang et al., 2021) to 0.01% (Hu et al., 2021), meaning a total fractionation of about 1.6%. On the other hand, it will be seen in this work that diffusive fractionation of  $^{41}\mathrm{K}/^{39}\mathrm{K}$  at high temperature can be much larger than 1.6%.

Diffusive isotope fractionation is due to isotope mass difference resulting in slightly different diffusivities. Both elemental and isotope fractionation can occur during diffusion. To evaluate diffusive elemental fractionation (e.g., Holycross and Watson, 2016), it is necessary to know the elemental diffusivities in a given melt at a given T-P condition. Zhang et al. (2010) and Zhang and Gan (2022) reviewed elemental diffusivities. Because diffusivity differences of different isotopes are small (often only a few percent or less), they typically cannot be resolved by directly measuring diffusivities of individual isotopes. Rather, the difference in diffusivities of isotopes is revealed by measuring isotope ratio profiles. If the diffusion of each isotope can be described by a single effective binary diffusivity, the diffusivity ratio of the heavy isotope ( $D_H$ ; note this is not diffusivity of hydrogen) to that of the light isotope  $(D_L)$ is obtained from experimental studies and used to predict isotope fractionation under different conditions. The background for this study and literature review can be found in Section 1 of the Supplementary File.

### 2. Experiments and SIMS analyses

Six experimental charges of diffusion couples with large K2O concentration contrast were chosen for this study from the many experimental charges of Guo and Zhang (2018, 2020). Details of the experiments are described in Guo and Zhang (2018, 2020). Relevant specifics are briefly summarized here. Starting glasses of the diffusion halves were synthesized using reagent chemicals and their compositions are listed as LHS and RHS in Table S1. The compositional variation in terms of absolute concentrations is small, no more than 3 wt% for each oxide. In preparing the low-K concentration side (LHS in Table S1), no  $K_2O$  was added. That is, the  $\sim 400$ ppm K<sub>2</sub>O in that half of the diffusion couple is from impurities in the reagent chemicals. The six experimental charges cover two series of diffusion couples (Table S1). Each series consists of three experiments (designated as A, B, C in the last letter of the Experiment# for experimental temperatures of 1350, 1500 and 1260 °C) of the same starting compositions on the two halves but different temperatures. One series (BS13&14A,B,C) has initial compensating concentration gradients mainly in SiO2 and K2O, and is hence referred to as the Si-K series or Si-K interdiffusion couples. The other series (BS17&18A,B,C) has initial compensating concentration gradients mainly in MgO and K2O, and is hence referred to as the Mg-K series, or Mg-K interdiffusion couples. The two series are used to examine the effect of the counter-diffusing oxide on the value of the empirical parameter  $\beta$  defined below (Richter et al., 1999):

$$\frac{D_{\rm H}}{D_{\rm L}} = \left(\frac{m_{\rm L}}{m_{\rm H}}\right)^{\beta},\tag{1}$$

where  $m_{\rm H}$  and  $m_{\rm L}$  are the atomic masses of the heavy and light isotopes. See Supplementary File for background of Equation (1). The initial compositions of the diffusion couples and the experimental conditions are listed in Tables S1 and S2 in the Supplementary File.

The  $^{41}$ K/ $^{39}$ K isotope ratio measurements were made using CAMECA IMS 7f-Geo ion microprobe (SIMS) at Caltech Microanalysis Center. Samples were first coated with a 20 nm layer of gold to make the surface conductive. A -13.5 keV  $^{16}$ O $^{-}$  primary ion beam was used to sputter the samples to generate secondary ions. The primary beam currents ranged from 0.20 nA to 10.5 nA, with increasing current at lower K2O concentrations in the samples. Each analysis position was pre-sputtered with a  $\sim$ 1 nA primary beam rastering over an area of 7  $\times$  7  $\mu$ m for 60 s. Data were

then collected with selected beam currents over a shrunk rastering size of 5  $\times$  5  $\mu m$ . Secondary ions of  $^{41}K^+$  and  $^{39}K^+$  of 9 keV were counted in the peak-jumping mode with an electron multiplier (EM) and corrected for the EM deadtime. The mass resolving power of the mass spectrometer was set at 4000, sufficient for removing any significant interference to  $^{39}K^+$  and  $^{41}K^+$ . During each peak-jumping cycle, the counting times were 1 s for  $^{39}K$  and 8 or 4 s for  $^{41}K$  (see Section 3 in the Supplementary File on optimal counting time), with 1 s magnet settling ('waiting') time before each counting. Each data point consists of 30 to 180 cycles, depending on the  $K_2O$  concentration.

Various measurement conditions (mostly beam currents) and procedures were explored to optimize the analysis precision in different sessions from 2018 to 2021. During and after each session, effort was made to understand the data and to improve the procedure with various ideas for the next session so as to improve the precision. Because of the continued effort to improve the precision, earlier  $\delta^{41} {\rm K}$  data have greater uncertainties (up to 2‰, one standard deviation hereafter) but were still used. More recent data have uncertainties down to 0.2‰. The final optimized measurement procedures are as follows:

- (1) Using different beam currents (e.g., 0.5, 0.2, 0.1 nA) to measure  $\delta^{41} \rm K$  in a small area at the far-field of high-K side to determine the deadtime so that  $\delta^{41} \rm K$  is constant.
- (2) Using a beam current of  $\sim$ 0.4 nA (which generates close to  $10^6$  counts of  $^{39}$ K per second) and about 20 minutes total counting time, to analyze  $\delta^{41}$ K for the whole profile. This profile provides high precision data of  $\delta^{41}$ K (approaching 0.2‰) at high-K concentration and the full concentration profile of K<sub>2</sub>O when using EMPA data at the high-K side as calibration. The SIMS concentration profile at a fixed beam current provides a more precise initial concentration contrast for modeling isotope diffusion. This is necessary because EMPA data for K<sub>2</sub>O at 0.04 wt% have a relative uncertainty of 15% to 20%, leading to large uncertainty in the initial concentration ratio.
- (3) For the low-K concentration side, remeasure  $\delta^{41}$ K at selected points using higher beam current and longer counting time to achieve a high enough precision (about 0.4%).
- (4) Remeasure  $\delta^{41} K$  at a few points at the high-K side to check whether there is drift.

In addition, the optimal time ratio for counting  $^{41}$ K (the less abundant isotope) and  $^{39}$ K (the more abundant isotope) is not the inverse abundance ratio (93.2581/6.7302) = 13.9, but is theoretically determined to be the square root of the inverse abundance ratio (93.2581/6.7302) $^{1/2}$  = 3.7 (Section 3 in the Supplementary File). Hence, a counting time of 1 s for  $^{39}$ K and 4 s for  $^{41}$ K was used so as to optimize the counting precision of the measured isotope ratio for a given total time of measurement.

The deadtime for correcting the counts was determined in 2020 and 2021 SIMS sessions but not in the 2018 session. For the 2018 session, the deadtime was chosen so that the isotope ratio profiles (especially the mean difference in isotope ratios at high-K and low-K far-fields) are consistent with later sessions.

The potassium isotope ratio is expressed using the  $\delta$ -notation as follows:

$$\delta^{41}K = \left(\frac{(^{41}K/^{39}K)_{SMP}}{(^{41}K/^{39}K)_{STD}} - 1\right)1000\%, \tag{2}$$

where  $(^{41}\text{K}/^{39}\text{K})_{\text{SMP}}$  is the ratio measured at a given point in the sample, and  $(^{41}\text{K}/^{39}\text{K})_{\text{STD}}$  is the ratio in the standard (two standards have been used in the literature, Teng et al., 2017). To determine diffusive fractionation of the  $^{41}\text{K}/^{39}\text{K}$  ratio (the  $\beta$  factor), the absolute ratios are not important; only the relative variations are. Hence, no  $^{41}\text{K}/^{39}\text{K}$  isotope ratio standard is used in this study, and  $(^{41}\text{K}/^{39}\text{K})_{\text{STD}}$  is taken to be the ratio at the high-K<sub>2</sub>O concentration

side, which agrees with the nominal  $^{41}$ K/ $^{39}$ K ratio (Berglund and Wieser, 2011) within  $\pm 2.4\%$ , as will be shown in Results).

### 3. Results

Among the six diffusion couples measured by SIMS, five are free of cracks, and one (BS17&18A) has a large (about 90  $\mu m$  wide) horizontal crack near the interface. The distance across the crack is corrected using the same correction as in Guo and Zhang (2018). The SIMS data are used to obtain not only the  $^{41} \text{K}/^{39} \text{K}$  isotope ratios, but also the K2O concentration profiles assuming negligible matrix effect (Section 4 in the Supplementary File). The concentration data from SIMS  $^{39} \text{K}$  counts have very high precision, and are in general consistent with EMPA data. However, for sample BS17&18C, the SIMS data reveal significant inconsistency with the EMPA data, indicating inhomogeneity at the high-K far-field (Fig. S2).

## 3.1. ${}^{41}K/{}^{39}K$ isotope ratio at high-K side

Measured  $^{41}$ K/ $^{39}$ K ratios in the high-K side are used to gauge the precision and accuracy of the isotope ratio measurements, as well as possible Soret-effect in K isotope distribution. The data show that  $^{41}$ K/ $^{39}$ K ratio at the high-K side from a single day-night session display no trend with distance, and can be regarded as constant within error. The error on the  $^{41}$ K/ $^{39}$ K ratio based on reproducibility at the high-K far-field ranges from 0.17% to 0.64%, and earlier data had larger error. Hence, if there is any Soret effect in K isotope diffusion, it is smaller than the measurement error.

Richter et al. (2014) reported that the Soret effect for  $\delta^{41} \text{K}/^{39} \text{K}$  in molten basalt is 2.1% per 100 °C. In this study, the total temperature variation in the measured far-field (usually about 500 µm to 1000 µm from the center) of the experimental samples is 4 to 7 °C calculated using the temperature calibration in Hui et al. (2008). Hence, the maximum Soret effect is  $\sim$ 0.15%, which is smaller than the standard deviation of the measurements. That is, the negligible Soret effect in K isotope diffusion observed in this study is in agreement with literature results.

The overall average  $^{41}$ K/ $^{39}$ K ratio of all sessions at high-K farfield is 0.072157  $\pm$  0.000122, similar to the nominal  $^{41}$ K/ $^{39}$ K ratio (6.7302/93.2581 = 0.072167, Berglund and Wieser, 2011), differing by only ( $-0.14 \pm 1.70$ )‰. However, the average  $^{41}$ K/ $^{39}$ K ratio in the high-K far-field in a single day-night session can differ from the nominal ratio by -2.3% to +2.4% from another day (Fig. 1). One sample (BS17&18C) was analyzed in all three sessions in 2018, 2020, and 2021, and the average  $\delta^{41}$ K/ $^{39}$ K ratio in the high-K farfield in different sessions is  $+1.5 \pm 0.6$ ,  $-2.3 \pm 0.2$ ,  $+(2.1 \pm 0.2)\%$ , essentially covering the whole range of variability. Hence, the variation in the average  $^{41}$ K/ $^{39}$ K ratio in the high-K far-field is not due to difference in the true  $^{41}$ K/ $^{39}$ K ratio in different samples, even though these offsets from the nominal ratio are much larger than the reproducibility in a single day-night session. They are attributed to different machine fractionation due to subtle day-to-day differences in SIMS operating conditions.

In summary, using SIMS, the absolute  $^{41}$  K/ $^{39}$ K isotope ratio in basalt glass can be measured to an accuracy of better than 2.5%. The long-term average of the absolute  $^{41}$  K/ $^{39}$ K isotope ratio at high-K side is essentially the same as the nominal ratio. Hence, the  $^{41}$  K/ $^{39}$ K ratio in the high-K far-field of diffusion couples in this study is assumed to be a constant and is used as the normalization standard in calculating  $\delta^{41}$ K. That is, the high-K far-field is defined as  $\delta^{41}$ K = 0. The relative precision of the isotope ratio along a profile in a single day-night session can have much higher precision, with  $1\sigma$  error of about 0.6% in earlier measurements, improving to about 0.2% in later measurements. For the low-K far-field, the small amount of  $K_2O$  was from impurities with unconstrained

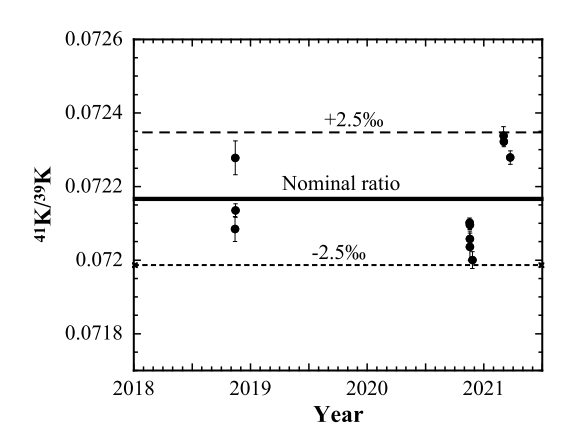


**Fig. 1.** Measured  $^{41}\text{K}/^{39}\text{K}$  ratio at the high-K far-field in this study (solid circles with  $1\sigma$  error bars) compared to the nominal  $^{41}\text{K}/^{39}\text{K}$  ratio (Berglund and Wieser, 2011). The upper and lower horizontal dashed lines represent 2.5‰ deviation from the nominal ratio.

 $\delta^{41}$ K. Hence, in fitting  $\delta^{41}$ K profiles,  $\delta^{41}$ K at the low-K far-field is allowed to be different from zero.

# 3.2. $^{41}K/^{39}K$ isotope ratio profiles

One example of  $\delta^{41} \text{K}/3^9 \text{K}$  profiles is shown in Fig. 2, together with K<sub>2</sub>O concentration profiles for comparison. All isotope ratio profiles with fits are shown in Figs. S3 and S4 in the Supplementary File. At the high K concentration side, there is a small  $\delta^{41} \text{K}$  maximum. At the low K concentration side, there is a large  $\delta^{41} \text{K}$  minimum. The maximum and minimum are as expected and can be understood as follows. As K diffuses from high concentration to low concentration, due to smaller mass of  $^{39} \text{K}$  compared with  $^{41} \text{K}$ ,  $^{39} \text{K}$  diffuses more rapidly. Hence, at the high K concentration side, there is  $^{39} \text{K}$  deficiency, leading to a maximum in  $\delta^{41} \text{K}$ . At the low K concentration side, there is extra  $^{39} \text{K}$ , leading to a minimum in  $\delta^{41} \text{K}$ . The minimum at the low concentration side is larger because a given amount of extra  $^{39} \text{K}$  would have a larger effect on  $\delta^{41} \text{K}$  at the side of lower initial K concentration.

# 4. Discussion

# 4.1. Modeling the $K_2O$ and $^{41}K/^{39}K$ diffusion profiles

Initially, constant EBDC values were assumed to model the  $\rm K_2O$  concentration profiles and  $^{41}\rm K/^{39}\rm K$  ratio profiles (Fig. 2). Adopting constant EBDC, the concentration profiles of each of  $^{41}\rm K$  and  $^{39}\rm K$  would be an error function. The isotope ratio  $^{41}\rm K/^{39}\rm K$  can be expressed as follows:

$$\frac{^{41}\text{K}}{^{39}\text{K}} = \frac{0.5(C_{41,\text{LHS}} + C_{41,\text{RHS}}) + 0.5(C_{41,\text{RHS}} - C_{41,\text{LHS}}) \text{ erf } \frac{x - x_0}{\sqrt{4D_{41}t}}}{0.5(C_{39,\text{LHS}} + C_{39,\text{RHS}}) + 0.5(C_{39,\text{RHS}} - C_{39,\text{LHS}}) \text{ erf } \frac{x - x_0}{\sqrt{4D_{39}t}}},$$
(3)

where  $x_0$  is the interface position, x increases from LHS to RHS, and subscripts 41 and 39 mean  $^{41}$ K and  $^{39}$ K. Converting to the  $\delta$ -notation and using the initial ratio at the RHS as standard lead to:

$$\delta^{41}K = \begin{cases} \frac{[(1+\delta_{LHS})+R]+[R-(1+\delta_{LHS})]\operatorname{erf}\frac{x-x_0}{\sqrt{4(m_{39}/m_{41})^{\beta}D_{39}t}}}{(1+R)+(R-1)\operatorname{erf}\frac{x-x_0}{\sqrt{4D_{39}t}}} \\ -1 \end{cases} 1000\%, \tag{4}$$

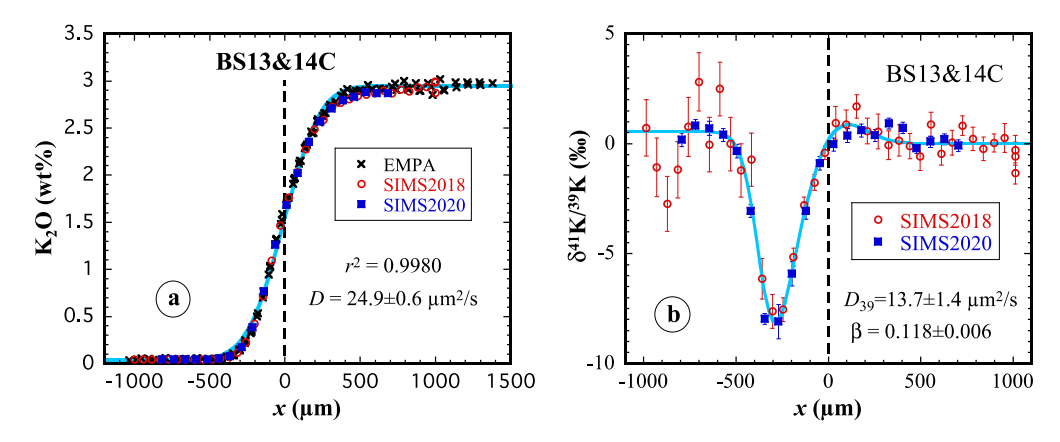


Fig. 2. Concentration and isotope ratio profiles fit using constant effective binary diffusion coefficient (EBDC). (a) EMPA data and two sets of SIMS data for  $K_2O$  concentrations are fit together using an error function to obtain EBDC for chemical diffusion of  $K_2O$ . (b) Two sets of SIMS data for  $\delta^{41}$ K are fit together using Equation (4) to obtain  $D_{39}$ . For easiness to follow, EMPA data are represented by black x, SIMS2018 data are represented by red open circles, SIMS2020 data are represented by blue solid squares, and SIMS2021 data are represented by purple +. Fit curves of combined two or more data sets are in teal color. (For interpretation of the colors in the figure(s), the reader is referred to the web version of this article.)

where  $R=C_{RHS}/C_{LHS}$  is the initial concentration ratio of the RHS to the LHS (or concentration contrast) and  $\delta_{LHS}$  (note that  $\delta_{LHS}=1\%$  means that  $\delta_{LHS}=0.001$ ) is  $\delta^{41}$ K at the initial LHS (recall that  $\delta_{RHS}$  is defined to be zero).

Assuming constant EBDC for  $K_2O$  seems to fit  $K_2O$  concentration profiles by EMPA and SIMS well (Guo and Zhang, 2018, 2020). An example can be seen in Fig. 2a. The isotope ratio profiles can also be fit well (Fig. 2b). However, the EBDC from  $K_2O$  concentration profile may be significantly larger than that from  $\delta^{41}K$  profile in the same experiment. For example, Fig. 2 shows that EBDC from the  $K_2O$  concentration profile is almost 2 times that from the  $\delta^{41}K$  profile. What is the reason for this discrepancy?

I first tried to understand the large difference in extracted D values from concentration and  $\delta^{41} K$  profiles as multicomponent diffusion effect. However, preliminary treatment by incorporating multicomponent effects using the theory in Watkins et al. (2014) was not successful (Section 6a in the Supplementary File) unless K isotope cross diffusivities are much larger than  $D_{39}$ . Hence, effort was made to assess other possibilities.

Careful examination of the fit of the concentration profiles in Fig. 2a reveals small but noticeable systematic misfit: at low  $K_2O$  concentrations, the data are steeper than the curve of constant D, which imply smaller D at lower  $K_2O$  concentrations; at high  $K_2O$  concentrations, the data are less steep than the curve, implying greater D value. The misfit of the  $K_2O$  concentration profile at low  $K_2O$  concentrations is better shown when using logarithm scale for concentration (Fig. 3).

The systematic misfits mean that K diffusivity increases with K concentration: smaller D at low concentrations and greater at high concentrations. It so happens that the  $\delta^{41}$ K shows the largest difference from the initial (also far-field) values at  $x \approx -300~\mu m$  (Fig. 2b), where K<sub>2</sub>O concentration is very low,  $\sim$ 0.14 wt%. Because curve fit tries to fit the variations of the data by adjusting fitting parameters, the diffusivity from a fit of the isotope ratio profiles is largely determined by data that show largest variation from the far-field values. That is,  $D_{39}$  in Fig. 2b largely reflects the  $D_{\rm K}$  value at K<sub>2</sub>O  $\approx$  0.14 wt%, whereas D in Fig. 2a reflects  $D_{\rm K}$  at about the average K<sub>2</sub>O, which is  $\sim$ 1.5 wt%. The two diffusivities can hence be significantly different if  $D_{\rm K}$  depends on K<sub>2</sub>O concentration.

To reconcile the apparent difference in  $D_{\rm K}$  and  $D_{39}$ , it is necessary to use concentration-dependent diffusivity to fit both the concentration and the isotope ratio profiles. A MatLab program was written to fit the concentration profiles numerically, and another program was written to fit the isotope ratio profiles numerically.

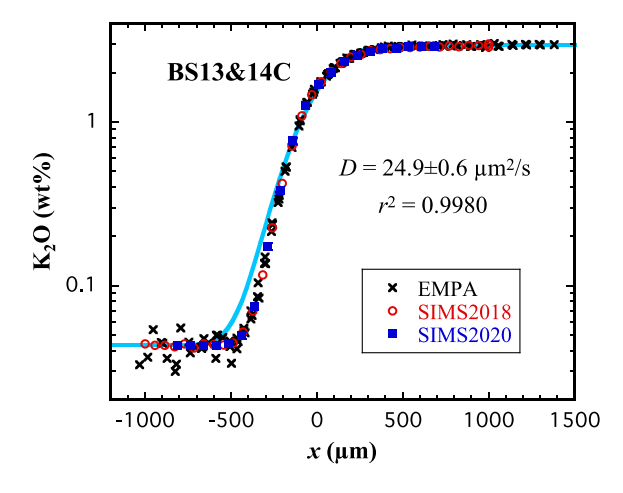


**Fig. 3.** The same data and fit as in Fig. 2a, but the vertical axis is now logarithm scale so that the misfit at low concentrations can be clearly seen.

The effective binary diffusivity is assumed to depend exponentially on K<sub>2</sub>O concentration:

$$D_{K_2O} = D_1 \exp(aC), \tag{5}$$

where C is  $K_2O$  concentration in wt%, and  $D_1$  and a are two fitting parameters ( $D_1$  is  $K_2O$  diffusivity at zero  $K_2O$  concentration). Least squares fitting of concentration profiles is carried out to minimize

$$\chi^2 = \sum_{i} \left( \frac{C_{i,\text{meas}} - C_{i,\text{calc}}}{\sigma_i} \right)^2, \tag{6}$$

where  $\sigma_i$  values are interpolated based on standard deviation of measured points on the low- $K_2O$  and high- $K_2O$  far-fields, and  $C_{i,\text{calc}}$  depends on fitting parameters  $D_1$  and a. In fitting the isotope ratio profiles,  $D_{39}$  is assumed to have the same expression as  $D_{K_2O}$  in Equation (5), and the parameter a is fixed to be the same as that from fitting the concentration profiles so that  $D_1$  values can be compared. The  $D_1$  values for  $^{39}K$  and  $^{41}K$  are related by Equation (1). Fig. 4 shows the fits to both concentration profiles and isotope ratio profiles of BS13&14C. It can be seen that the fit to the concentration profile (Fig. 4a) has no noticeable misfits and is much better than the fit in Fig. 3 (which assumes constant D). The improvement in the fitting can be quantified from  $1-r^2$  value. When constant D is used,  $1-r^2=0.0020$  (Fig. 3), meaning 0.2% of data variation is not accounted for. On the other hand,

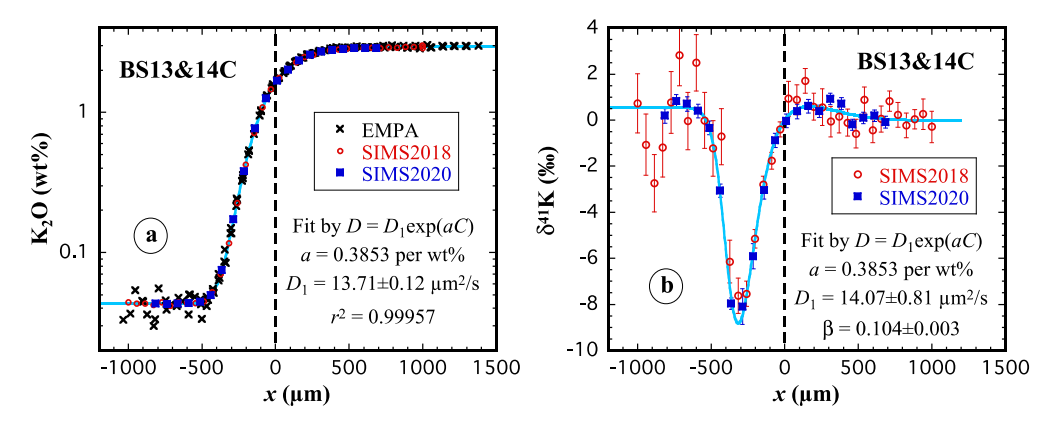


**Fig. 4.** K<sub>2</sub>O concentration profile and  $\delta^{41}$ K profile in experiment BS13&14C fit by concentration-dependent diffusivity as  $D = D_1 \exp(aC)$  where C is K<sub>2</sub>O concentration in wt%, and  $D_1$  and  $D_2$  are two parameters. For easy comparison, the value of  $D_2$  in fitting the  $D_2$  fitting the same as that from fitting the concentration profile. All errors and error bars are one standard deviation.

**Table 1** Fitting results assuming  $D = D_1 \exp(aC)$ .

Exp#	T (°C)	Fit K <sub>2</sub> O profiles (EMPA+SIMS)			Fit <sup>41</sup> K profiles		
		a (wt% <sup>-1</sup> )	$D_1 (\mu m^2/s)$	MSWD	$D_1  (\mu \text{m}^2/\text{s})$	β	MSWD
BS13&14C	1260	$0.385 \pm 0.011$	$13.71 \pm 0.12$	0.61	$14.07 \pm 0.81$	$0.104 \pm 0.003$	1.08
BS13&14A	1350	$0.297\pm0.014$	$29.4 \pm 0.3$	1.55	$36.5 \pm 2.2$	$0.108 \pm 0.004$	1.56
BS13&14B	1500	$0.175\pm0.015$	$99.9 \pm 1.6$	3.46	$124 \pm 7.4$	$0.116 \pm 0.003$	2.78
BS17&18Ca	1260	$0.175\pm0.018$	$16.11 \pm 0.40$	1.46	$21.8 \pm 1.4$	$0.117 \pm 0.003$	2.85
BS17&18A	1350	$0.144 \pm 0.015$	$24.7 \pm 0.37$	3.16	$25.0 \pm 2.5$	$0.090 \pm 0.005$	1.89
BS17&18B	1500	$0.078\pm0.012$	$78.4 \pm 0.7$	1.71	$86.2 \pm 8.3$	$0.0997\pm0.0035$	2.55

Notes:  $K_2O$  concentration data are from Guo and Zhang (2018, 2020) for EMPA data and this work for SIMS data. C in  $\exp(aC)$  is  $K_2O$  concentration in wt%. Hence, the unit of a is wt% $^{-1}$ . Errors are fitting errors at one standard deviation.

<sup>a</sup> There is significant initial heterogeneity at the high  $K_2O$  side for BS17&18C, which could be the cause for the somewhat outlier results

when D is assumed to increase with  $K_2O$  concentration exponentially,  $1-r^2=0.00043$  (Fig. 4a), meaning only 0.043% of total data variation is not accounted for. The quality of the fit to the isotope ratio profiles is also improved although not easily seen. In addition, the diffusivity from  $\delta^{41}K$  profiles is in agreement within error with that from K concentration profiles.

Consequently, the concentration profiles (combining EMPA and SIMS) and isotope ratio profiles (combining different SIMS sessions) of all six experiments are fit by assuming  $D_{\rm K_2O} = D_1 \exp(aC)$ . All fits are shown in Figs. S3 and S4 in the Supplementary File, and fitting results are summarized in Table 1.

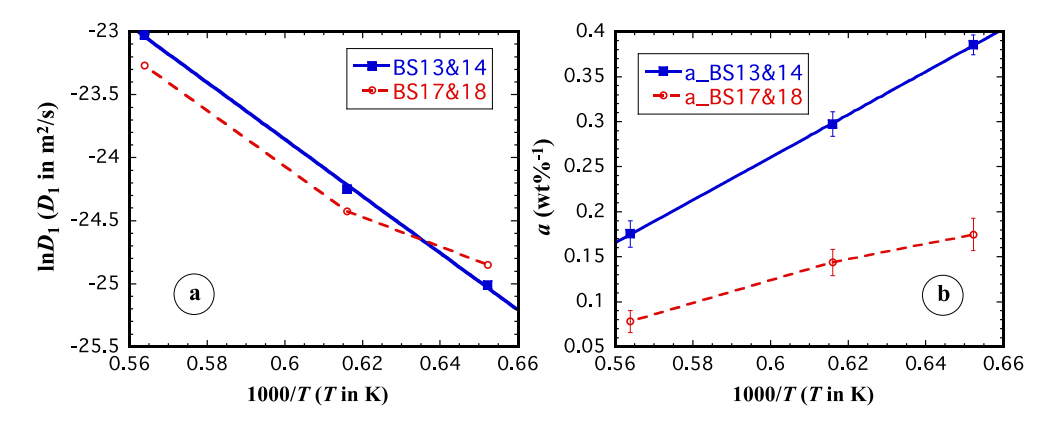
The fitting results in Table 1 show that the error on  $D_1$  based on  $^{41}$ K/ $^{39}$ K isotope ratio profiles is larger than that based on the K $_2$ O concentration profiles. Hence, even though the isotope ratio profiles can constrain the difference between  $D_{39}$  and  $D_{41}$  much better than using the concentration profiles, the concentration profiles can actually constrain the absolute values of  $D_{K}$  (similar to  $D_{39}$ ) much better, with errors about 1/7 of those from isotope ratio fits.

Fig. 5a displays the dependence of  $D_1$  on temperature on an Arrhenius plot. For the BS13&14 series (Si-K interdiffusion couples), there is an excellent Arrhenius relation. However, for the BS17&18 series (Mg-K interdiffusion couples), the point at the lowest temperature (BS17&18C) is off. The sample BS17&18C shows the largest discrepancy between EMPA and SIMS data and there is noticeable heterogeneity of  $K_2O$  concentration at the high- $K_2O$  far-field (Fig. S2 in the Supplementary File). Hence, there are systematic concentration deviations that cannot be captured by the fitting, which might be the reason that the fitted results are off.

The parameter a from the fitting characterizes how strongly K diffusivity depends on  $K_2O$  concentration. This parameter is plotted in Fig. 5b, and it decreases with increasing temperature for both Si-K and Mg-K diffusion couples. For the Si-K diffusion cou-

ples (BS13&14 series), there is an excellent linear relation between a and 1000/T. However, for the Mg-K diffusion couples, the linear relation is worse. The decrease of a with T means that the temperature dependence of  $K_2O$  effective binary diffusivity is weaker at higher temperatures, as expected.

The variation of  $\beta$  with temperature is shown in Fig. 6. The  $\beta$  value ranges from 0.09 to 0.116. Many exchanging diffusion mechanisms would produce similar  $\beta$  values, including: NaKO exchanging with CaO ( $\beta = 0.105$ ; calculated using Equation (S3) in the Supplementary File) or  $SiO_2$  ( $\beta = 0.109$ ),  $K_2O$  exchanging with  $NaAlO_2$  ( $\beta = 0.097$ ),  $KAlO_2$  exchanging with  $NaAlO_2$  ( $\beta = 0.091$ ) or Na<sub>2</sub>FeO<sub>2</sub> ( $\beta = 0.116$ ), and KAlSiO<sub>4</sub> exchanging with the network with fairly large M (e.g.,  $\beta = 0.108$  if M = 1000 amu). Because initial concentration gradients are mainly between K2O and SiO2 in the BS13&14 series, and between K2O and MgO in the BS17&18 series, the best match seems to be NaKO exchanging with SiO<sub>2</sub> ( $\beta = 0.109$ ) in the BS13&14 series, and NaKO exchanging with MgO ( $\beta = 0.085$ , just a little below the observed range) in the BS17&18 series. On the other hand, the diffusion mechanism of  $K_2O$  exchanging with  $SiO_2$  ( $\beta = 0.081$ ) and MgO ( $\beta = 0.063$ ) would lead to too small  $\beta$  values. The exchange diffusion mechanism of NaKO with SiO2 or MgO has its own difficulties. The initial Na2O concentration profile before these experiments was essentially flat (Guo and Zhang, 2018, 2020). Diffusion indeed resulted in Na<sub>2</sub>O uphill diffusion from high to low K<sub>2</sub>O side, which supports the diffusion of NaKO as a cluster. However, quantitatively, the molar amount of Na<sub>2</sub>O moved appears much smaller than that of K<sub>2</sub>O. For example, K2O concentration changed by 2.9 wt% across the profile, but the total variation in Na<sub>2</sub>O concentration is only  $\leq 0.6$ wt%. Not enough information is available to assess whether such differences can be accounted for by simultaneous diffusion and reaction (Zhang et al., 1991; Behrens et al., 2007).



**Fig. 5.** The dependence of  $\ln D_1$  and a on 1000/T for the two series of experiments (three experiments of BS13&14 are Si-K interdiffusion couples and those of BS17&18 are Mg-K interdiffusion couples). Error bars are 1 standard deviation based on the fitting. For  $\ln D_1$ , the error bars are smaller than the symbols.

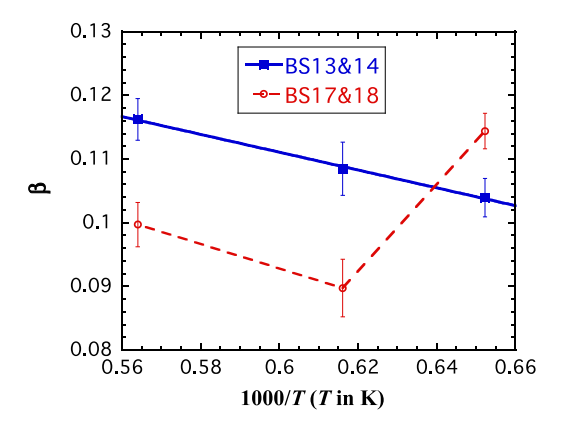


**Fig. 6.** The dependence of  $\beta$  on 1000/T. For the BS13&14 series (Si-K interdiffusion couples), there is excellent correlation between  $\beta$  on 1000/T. The equation for the linear fitting is:  $\beta=0.195-140/T$ . For the BS17&18 series (Mg-K interdiffusion couples), BS17&18C at  $1260\,^{\circ}\text{C}$  is off the trend, and the rest of the data are subparallel to the BS13&14 trend.

In summary, the  $\beta$  value increases with temperature, and from Mg-K couples to the Si-K couples. The increase of  $\beta$  value with temperature is opposite to expectation based on equilibrium isotope fractionation that becomes smaller as temperature increases. One explanation is that as temperature increases, the average size of the clusters for K diffusion decreases, leading to an increase in the  $\beta$  value. The slightly smaller  $\beta$  values for the Mg-K interdiffusion couples than for the Si-K couples is consistent with the smaller mass of MgO than SiO<sub>2</sub>.

The isotope ratio profiles of BS13&14C (the best data) have also been fit using diffusion matrix of Guo and Zhang (2018, 2020) by allowing  $D_{K,K}$  in the diffusion matrix to be mass dependent as in Equation (1). The treatment is summarized in Section 6b of the Supplementary File and resulted in a  $\beta_{K,K}$  value between 0.10 to 0.12. It did not yield better results or more insight than the effective binary diffusion treatment.

### 4.2. EBDC of K<sub>2</sub>O in basaltic melt during SiO<sub>2</sub>-K<sub>2</sub>O interdiffusion

The linear relations for parameters a and  $\ln D_1$  on 1000/T for the BS13&14 series (Si-K interdiffusion couples) are well constrained as shown in Fig. 5 and can be expressed as follows:

$$a = -(1.164 \pm 0.016) + (2374 \pm 26)/T,$$
 (7)

and

$$\ln D_1 = -(10.31 \pm 0.41) - (22565 \pm 664)/T, \tag{8}$$

where a is in wt%<sup>-1</sup>, T is temperature in K, and  $D_1$  is in m<sup>2</sup>/s (not  $\mu$ m<sup>2</sup>/s as in Table 1).

Combining Equations (7), (8), and (5), the effective binary diffusivity of  $K_2O$  in basaltic melt during  $SiO_2$ - $K_2O$  interdiffusion can be calculated as:

$$\ln D_{K_2O} = -10.31 - 22565/T + (-1.164 + 2374/T)C_{K_2O}, \qquad (9)$$

where  $C_{\rm K_2O}$  is  ${\rm K_2O}$  concentration in wt%. Because of the covariation of  ${\rm K_2O}$  and  ${\rm SiO_2}$  concentrations in interdiffusion couples, whether  ${\rm K_2O}$  EBDC actually increases with increasing  ${\rm K_2O}$  or decreases with increasing  ${\rm SiO_2}$  concentration or a combination of both needs further examination. As can be seen from Table 1 and Fig. 5b, the parameter a in the Mg-K couples is about half of that in the Si-K couples. Suppose the compositional variation of  $D_{{\rm K_2O}}$  in the Mg-K couples is entirely due to  ${\rm K_2O}$  concentration variation. Then,  ${\rm SiO_2}$  concentration variation accounts for at least half of the a value in the Si-K couples.

The effective binary diffusivity in basalt during interdiffusion depends strongly on the counter diffusion component (e.g., Guo and Zhang, 2016, 2018, 2020; Zhang and Gan, 2022). The relations in this subsection cannot be applied to, e.g., BS17&18 series experiments (MgO-K<sub>2</sub>O interdiffusion couples) or other interdiffusion couples. Because of data scatter mentioned earlier for the BS17&18 series, no effort is made to derive the general relation of  $D_{\rm K_2O}$  to temperature and K<sub>2</sub>O concentration.  $D_{\rm K_2O}$  in basaltic melt during Mg-K interdiffusion at about 1.5 wt% K<sub>2</sub>O may be roughly estimated by that during Si-K diffusion divided by 1.4 (Guo and Zhang, 2018, 2020). Because there is weaker dependence on K<sub>2</sub>O concentration,  $D_{\rm K_2O}$  during Mg-K interdiffusion at  $\leq$  0.2 wt% K<sub>2</sub>O is about 20% less than that during Si-K interdiffusion.

# 4.3. Comparison with literature data on diffusive isotope fractionation in silicate melts

The  $\beta$  factors from this study are here compared with literature data on different elements. Watkins et al. (2017) and Holycross et al. (2018) showed that the  $\beta_i$  parameter for i= Li, Mg, Ca, and Fe is roughly correlated with  $D_i/D_{\rm Si}$  where i is the element for which diffusive isotope fractionation is considered, and  $D_i$  and  $D_{\rm Si}$  are the EBDC of the element i and Si. In Fig. 7, the new data of  $\beta_{\rm K}$  are plotted in such a relation, and the rough correlation still holds. However, even though there is a rough correlation, about half of the variation in  $\beta_i$  (0.025 to 0.12) is in a very narrow range of  $D_i/D_{\rm Si}$  (between 1 and 2) and there is considerable scatter, making it difficult to predict  $\beta_i$  value in this  $D_i/D_{\rm Si}$  range. The scatter at  $D_i/D_{\rm Si}$  range of 1 and 2 may mean that a better relation is necessary, e.g., replacing  $D_{\rm Si}$  by the smallest eigenvalue of the diffusion

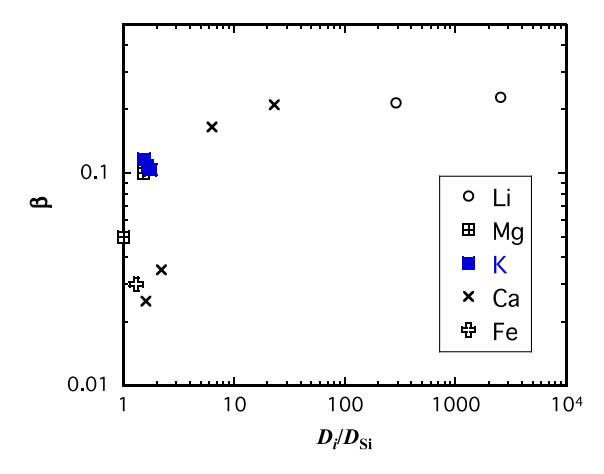


**Fig. 7.** The relation between  $\beta_i$  factor and  $D_i/D_{\text{Si}}$ .  $\beta$  values for K (blue solid squares) are from this work for the BS13&14 series ( $D_{\text{Si}}$  values are not available for the BS17&18 series), and other  $\beta$  values (black symbols) are from literature (Richter et al., 2003, 2008, 2009a; Watkins et al., 2009, 2011, 2017; Holycross et al., 2018).

matrix. However, not enough diffusion matrix data are available for such a treatment.

Next, diffusive K isotope fractionation in this study is compared with K isotope fractionation during Soret diffusion. Richter et al. (2014) found from experiments that K isotope fractionation in the presence of temperature contrast is about 1.06‰ per unit mass difference per 100 °C. That is,  $^{41}$ K/ $^{39}$ K isotope fractionation (the mass difference is 2) is about 2.1‰ per 100 °C. Using an average  $\beta$  value of 0.11, to produce the same magnitude of K isotope fractionation, a concentration ratio of 4.2 between the two sides of a diffusion couple is equivalent to a temperature difference of 100 °C, and a concentration contrast of 20 is equivalent to a temperature difference of 250 °C.

### 4.4. Diffusive K isotope fractionation during magmatic processes

The results in this study show that diffusive K isotope fractionation is likely observable in nature during magma mixing, such as mixing of tholeitic and alkali basalts, or basalt and rhyolite. For example, a tholeiitic basalt often contains 0.05 to 0.30 wt% K<sub>2</sub>O (Gale et al., 2013) and an alkali basalt may contain 1 to 2 wt% K2O (e.g., Azores, Jackson et al., 2012). Mixing of such two melts would have an initial K2O concentration ratio of 3 to 40. For the mixing of a rhyolite melt with about 5 wt% K<sub>2</sub>O (e.g., Hildreth, 1979; Hildreth et al., 1984), and a basalt melt with 0.05 to 2 wt%, the initial concentration ratio would range from 2.5 to 100. To simulate the isotope fractionation, the initial K isotopes in both melts are assumed to be the same with  $\delta^{41}K = 0$ . The effective binary diffusivity of K is expected to be variable and the exact functional form of the variation depends on the compositions of the two melts to be mixed. There might also be uphill diffusion (Sato, 1975; Watson, 1982; Zhang et al., 1989), which must be treated using a multicomponent diffusion approach. For simplicity, the complexities due to compositional dependence of diffusivity or uphill diffusion are ignored. To estimate the size of the isotope fractionation, ignoring compositional dependence of diffusivity may only lead to small errors. For example, Fig. 2b and Fig. 4b show that either constant D or concentration-dependent D can fit the isotope ratio profiles well and can reproduce the isotope ratio minimum at low-K<sub>2</sub>O side. However, to produce the same magnitude of isotope fractionation, a slightly larger  $\beta$  value is needed when D is constant compared with a concentration-dependent D. Here, for a nonspecific simulation, constant D is used. The empirical fractionation parameter  $\beta$ is taken to be 0.11 based on this work (Fig. 6).

Fig. 8 shows some simulation results for  $^{41}$ K/ $^{39}$ K fractionation. The maximum  $\delta^{41}$ K is less than 1‰ above the initial  $\delta^{41}$ K, and

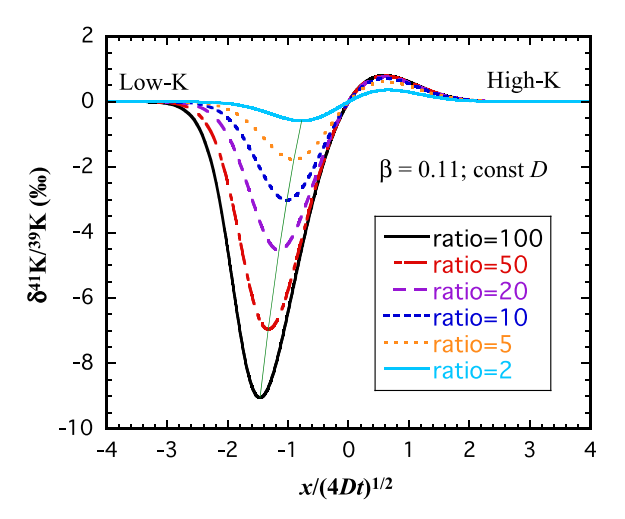


**Fig. 8.** Simulated diffusion-generated  $\delta^{41}$ K profiles. In the simulation,  $\beta$  is taken to be 0.11,  $D_{\rm K}$  is taken to be constant (hence the simulation is approximate), and initial  $\delta^{41}$ K is zero in both low-K and high-K side. Different curves are for different initial concentration ratios (defined to be  $C_{\rm K2O,RHS}/C_{\rm K2O,LHS}$ ). The horizontal axis is the normalized distance. The minimum  $\delta^{41}$ K occurs at  $x/(4Dt)^{1/2}\approx 1$ , but the exact position depends on the concentration ratio as shown by the thin green curve connecting the points of minimum  $\delta^{41}$ K in each curve.

hence difficult to resolve in nature. The minimum  $\delta^{41}$ K is fairly significant,  $\geq 3\%$  lower than the surrounding  $\delta^{41}$ K if the initial concentration ratio (defined to be  $C_{\rm K2O,high}/C_{\rm K2O,low}$ ) is greater than 10. The minimum  $\delta^{41}$ K value occurs at  $x \approx -2\alpha(Dt)^{1/2}$ , where the negative sign means that the minimum is at the side of lower-K concentration, and the parameter  $\alpha$  is of order 1 ( $\alpha$  = 0.78 for ratio = 2 and 1.47 for ratio = 100. Cooling might accompany diffusion during magma mixing, meaning that D may depend on time. In such cases, Dt in Fig. 8 should be replaced by  $\int Ddt$ , the integration of D with respect to time (Zhang, 2008). The presence of local  $\delta^{41}$ K anomaly (minimum) would be recorded by phenocrysts/crystals growing in the local melt.

The results in Fig. 8 are specific to  $^{41}$ K/ $^{39}$ K isotope fractionation during magma mixing. For the more general case of isotope fractionation during magma mixing, the total isotope fractionation  $\Delta$  (in ‰), defined as the extreme  $\delta$ -value at the positive x (RHS in Fig. 8), minus the extreme  $\delta$  at the negative x (LHS), is calculated and plotted in Fig. 9 as a function of  $R = C_{RHS}/C_{LHS}$  and  $D_H/D_L$ . Fig. 9 shows that  $\Delta$  is proportional to  $(1-D_H/D_L)$ . The dependence of  $\Delta$  on the ratio  $R = C_{RHS}/C_{LHS}$  is more complicated. After some effort, it is found that the following equation is able to roughly predict  $\Delta$  when  $D_H/D_L$  is between 1 to 0.94 and R is between 0.001 to 1000:

$$\Delta \approx Z (0.595 + 0.0918Z^2 - 0.004634Z^4) (1 - D_H/D_L) 1000\%, \tag{10}$$

where  $Z=\log_{10}$  R. The error of the above formula is  $\leq 0.01\%$  at  $\Delta=0.2\%$ ,  $\leq 0.1\%$  at  $\Delta=2\%$ ,  $\leq 1\%$  at  $\Delta=40\%$ ,  $\leq 3\%$  at  $\Delta=180\%$ . For example, using Equation (10) to predict the total isotope fractionation (from minimum to maximum) in Fig. 8 for a ratio of 10 leads to 3.75%, in good agreement with 3.72% in Fig. 8.

### 4.5. Significance in K-Ar or Ar-Ar dating

Diffusive K isotope fractionation is rather large (of the order 10% in this study). For mixing of tholeittic and alkali basalts or of basalt and rhyolite,  $^{41}$ K/ $^{39}$ K isotope ratio at the low-K<sub>2</sub>O side has a minimum, which may be significantly lower than the background

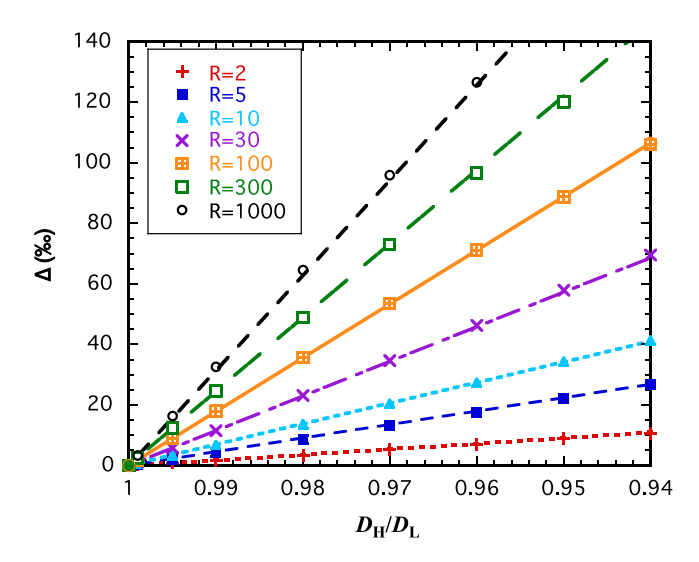


**Fig. 9.** Calculated total isotope fractionation  $\Delta$  (‰) across a diffusion couple profile during magma mixing as a function of  $D_{\rm H}/D_{\rm L}$  and R =  $C_{\rm RHS}/C_{\rm LHS}$ . The lines are calculated using Equation (10).  $D_{\rm H}/D_{\rm L}=(m_{\rm L}/m_{\rm H})^{\beta}$ . For  $^{41}{\rm K}/^{39}{\rm K}$  fractionation, taking  $\beta=0.11$  (this work),  $D_{\rm H}/D_{\rm L}=0.99451$ . For  $^{7}{\rm Li}/^{6}{\rm Li}$  fractionation, taking  $\beta=0.23$  (Holycross et al., 2018),  $D_{\rm H}/D_{\rm L}=0.9652$ .

 $^{41}$ K/ $^{39}$ K ratio. If a rock sample is collected from such a diffusion zone with  $\delta^{41}$ K of about -5%, then  $\delta^{40}$ K would be about -2.5%. In K-Ar dating, this would result in an error if the nominal  $^{40}$ K isotope abundance is used, rather than the fractionated  $^{40}$ K isotope abundance. As derived in Section 7 of the Supplementary File, the error in the calculated age ( $\Delta t = t_{\rm actual} - t_{\rm nominal}$ , where  $t_{\rm nominal}$  is the age using the nominal  $^{40}$ K abundance) would be

$$\Delta t \approx -\frac{1}{\lambda} \delta^{40} K \left[ 1 - \exp(-\lambda t_{\text{nominnal}}) \right]. \tag{11}$$

If  $\lambda t_{\text{nominal}} \ll 1$ , then the above equation is further simplified to:

$$\Delta t \approx -t_{\text{nominnal}} \delta^{40} \text{K}.$$
 (11a)

Note that if  $\delta^{40} K = 1\%$ , then  $\delta^{40} K = 0.001$  in the above equations. The approximation (11) works very well in all reasonable cases (e.g.,  $|\delta^{40} K| \leq 20\%$  for 2% relative precision in  $\Delta t$ ), whereas approximation (11a) works only for small ages (e.g.,  $t_{nominal} \leq 80$  Ma). Consider the dating of the Cretaceous-Paleogene boundary with  $t_{nominal} = 66.00$  Ma. If  $\delta^{40} K/\delta^{39} K = -2.5\%$ , then  $\Delta t \approx 0.16$  Ma, and  $t_{actual} \approx 66.16$  Ma. Renne et al. (2013) reported high-precision  $\delta^{40} K/\delta^{39} K = -2.5\%$  are the Cretaceous-Paleogene boundary, such as  $\delta 6.038 \pm 0.025/0.049$  Ma. The smallest error in their paper is 0.011 Ma at an age of  $\sim 66$  Ma. These stated errors can be much smaller than the errors caused by diffusive K isotope fractionation. Hence, for such high-precision dating, it is necessary to correct for the effect of diffusive K isotope fractionation in dating.

Observed variations in  $\delta^{41}$ K values in volcanic rocks so far are up to 1.6% (-1.55 to -0.32%, Wang et al., 2021; -0.66 to +0.01%, Hu et al., 2021). These variations may be due to kinetic (such as diffusive) or equilibrium fractionation. Take the case of  $\delta^{41}$ K difference of 1.6%. Then  $\delta^{40}$ K difference would be about 0.8%. Such fractionation would result in an age difference of 0.052 Ma for a rock with a nominal age of 66 Ma, greater than the reported error in some ages in Renne et al. (2013). Hence, it is also necessary to correct for such isotope fractionation in high-precision dating.

### 4.6. Diffusive K isotope fractionation during volatile loss of the Moon

The Moon is depleted in many volatile elements compared to the Earth (Lunar Sample Prelliminary Examination Team, 1969;

Hauri et al., 2015; Zhang, 2020), including K, which is depleted by a factor of  $\sim$ 5 (McDonough et al., 1992). In addition,  $^{41}$ K/ $^{39}$ K ratio in lunar mantle-derived basalts is slightly greater than terrestrial counterparts by about 0.4% (Wang and Jacobsen, 2016). The depletion of volatile elements and the very small enrichment of heavy isotopes in the Moon relative to the Earth are often attributed to volatile loss during planetary accretion (Wang and Jacobsen, 2016). Exactly how the depletion occurred leading to the isotope enrichment is still uncertain (Wang and Jacobsen, 2016; Zhang, 2020; Neuman et al., 2022). For example, Neuman et al. (2022) examined K isotope fractionation during evaporation and ruled out kinetic evaporation as the cause of the small K isotope difference because it would have resulted in too large fractionation in K isotopes than observed between the Moon and the Earth. Here the role of diffusive fractionation is explored using the  $\beta$  parameter obtained in this study.

The Moon is a fairly large planetary body, diffusive volatile loss is unlikely important for the whole Moon. Nonetheless, in the Giant impact hypothesis (Hartman and Davis, 1975; Cameron and Ward, 1976; Canup, 2004), volatile loss might have happened in the small blobs that were ejected during the Giant Impact and then collected to form the Moon. In this subsection, the isotope effect of diffusive loss of K from small spherical blobs (e.g., km-size) at high temperature is examined. It is assumed that the spherical blobs were (i) initially uniform in K concentration with  $\delta^{41}K = 0$ and (ii) losing K into either vacuum or an atmosphere that does not contain K. Assumption (ii) means that surface K concentration is zero. Without assumption (ii), the surface K concentration and whether it varied with time must be specified. However, there is not enough information for such specification. The following assumptions affect the time scale of the processes but do not affect the degree of K isotope fractionation at 80% K loss: (1) The spherical blobs had a radius of 1 km; (2) the initial temperature was 3000 K (which may be regarded as an average temperature of ejected blobs during Giant Impact, Canup, 2004), leading to K diffusivity at 0 to 300 ppm concentration level being about  $1.8 \times 10^{-8}$ m<sup>2</sup>/s based on Equation (9). Using Equation (S26) in the Supplementary File, in 0.2 Myr, the concentration of K in the blob would be decreased by a factor of 5. Given  $\beta = 0.11$  (not extrapolated to 3000 K, which would lead to a greater  $\beta$  and larger  $\delta^{41}$ K increase),  $\delta^{41}$ K in the whole blob would increase by 6.3\%. To produce the observed 0.4% fractionation in  $^{41}\text{K}/^{39}\text{K}$  ratio at 80% loss of K by diffusion would require a  $\beta$  value of 0.007, smaller than the observed  $\beta$  value by more than an order of magnitude.

The time scale of 0.2 Myr obtained from a pure diffusion model is likely too long and the blobs almost certainly cooled down much more rapidly even in the presence of an enveloping atmosphere (Wang and Jacobsen, 2016). Vigorous interior convection and surface boundary layer diffusion would accomplish the same degree of volatile loss in much shorter times. Using Equation (S29), incorporation of interior convection and surface boundary layer diffusion would increase  $\delta^{41} K$  to 8.9% at 80% K loss. The magnitude of K isotope fractionation at 80% K loss is independent of the boundary layer thickness but the time needed for 80% K loss is proportional to the boundary layer thickness. Therefore, it does not seem that diffusive or convective-diffusive K loss into a Kfree atmosphere can explain the observed difference in lunar and terrestrial K isotope ratios. A possible explanation of the observed small K isotope fractionation between the Moon and the Earth is near-equilibrium K loss (Neuman et al., 2022) into an atmosphere containing an appropriate and time-dependent concentration of K.

## 5. Conclusions

This study reports diffusive K isotope fractionation profiles in Si-K and Mg-K diffusion couples in multicomponent diffusion ex-

periments of Guo and Zhang (2018, 2020). The initial concentration ratio between high-K<sub>2</sub>O side and low K<sub>2</sub>O side is about 70. The magnitude of diffusive fractionation (difference between maximum and minimum  $\delta^{41} K/^{39} K$ ) in the diffusion couples is of the order 10%. Initial fitting assuming concentration-independent effective binary diffusivity shows a difference of a factor of  $\sim$ 2 in the effective binary diffusivity of K obtained from concentration and isotope ratio profiles. This difference can be reconciled by including concentration dependence of the effective binary diffusivity of K. The empirical isotope fractionation parameter  $\beta$  is found to be about 0.11 at 1373 °C for the Si-K series, and increases slightly with increasing temperature. For the Mg-K series, if an outlier point is excluded, the  $\beta$  value is lower by  $\sim$ 0.017 than that for the Si-K series. These  $\beta$  parameters are roughly consistent with a diffusion mechanism of NaKO exchange with SiO2 for the Si-K series, and NaKO exchange with MgO for the Mg-K series. It is predicted that diffusive K isotope fractionation during magma mixing is measurable by conventional mass spectrometry and SIMS. In addition, it is necessary to measure K isotope ratios in high-precision K-Ar age determination. Calculations show that the observed  $\delta^{41}$ K enrichment in the Moon relative to the Earth is much smaller than the calculated enrichment if it were due to diffusion-controlled K loss into a K-free atmosphere.

### **CRediT authorship contribution statement**

**Youxue Zhang:** Conceptualization, Methodology, Data collection, Validation, Modeling, Programming, Writing.

### **Declaration of competing interest**

The authors declare that they have no known competing financial interests or personal relationships that could have appeared to influence the work reported in this paper.

### Acknowledgement

This work was supported by NSF grants EAR-1829822 and EAR-2020603 and NASA grant 80NSSC19K0782. I greatly appreciate the technical help by Dr. Yunbin Guan of Caltech Microanalysis Center. I thank Dr. Ting Gan who participated in the early stage of this project, and Dr. James Watkins for the suggestion to look at diffusive isotope fractionation in our diffusion experiments. Constructive comments by two anonymous reviewers significantly improved the quality of this work.

# Appendix A. Supplementary material

Supplementary material related to this article can be found online at https://doi.org/10.1016/j.epsl.2022.117405.

### References

- Behrens, H., Zhang, Y., Leschik, M., Miedenbeck, M., Heide, G., Frischat, G.H., 2007. Molecular H<sub>2</sub>O as carrier for oxygen diffusion in hydrous silicate melts. Earth Planet. Sci. Lett. 254, 69–76.
- Berglund, M., Wieser, M.E., 2011. Isotopic compositions of the elements 2009. (IUPAC Technical Report). Pure Appl. Chem. 83, 397–410.
- Cameron, A.G.W., Ward, W.R., 1976. The origin of the moon. Lunar Planet. Sci. Conf. 7, 120–122.
- Canup, R.M., 2004. Simulations of a late lunar-forming impact. Icarus 168, 433–456. Chopra, R., Richter, F.M., Watson, E.B., Scullard, C.R., 2012. Magnesium isotope fractionation by chemical diffusion in natural settings and in laboratory analogues. Geochim. Cosmochim. Acta 88, 1–18.
- Gale, A., Dalton, C.A., Langmuir, C.H., Su, Y., Schilling, J.G., 2013. The mean composition of ocean ridge basalts. Geochem. Geophys. Geosyst. 14. https://doi.org/10.1029/2012GC004334.
- Guo, C., Zhang, Y., 2016. Multicomponent diffusion in silicate melts: SiO<sub>2</sub>-TiO<sub>2</sub>-Al<sub>2</sub>O<sub>3</sub>-MgO-CaO-Na<sub>2</sub>O-K<sub>2</sub>O system. Geochim. Cosmochim. Acta 195, 126–141.

- Guo, C., Zhang, Y., 2018. Multicomponent diffusion in basaltic melts at 1350°C. Geochim. Cosmochim. Acta 228, 190–204.
- Guo, C., Zhang, Y., 2020. Multicomponent diffusion in a basaltic melt: temperature dependence. Chem. Geol. 549.
- Hartman, W.K., Davis, D.R., 1975. Satellite-sized planetesimals and lunar origin. Icarus 24, 504–515.
- Hauri, E.H., Saal, A.E., Rutherford, M.J., Van Orman, J.A., 2015. Water in the moon's interior: truth and consequences. Earth Planet. Sci. Lett. 409, 252–264.
- Hildreth, W., 1979. The Bishop Tuff: Evidence for the Origin of Compositional Zonation in Silicic Magma Chambers. Geol. Soc. Am. Spec. Paper, vol. 180, pp. 43–73.
- Hildreth, W., Christiansen, R.L., O'Neil, J.R., 1984. Catastrophic isotopic modification of rhyolitic magma at times of caldera subsidence, Yellowstone Plateau volcanic field. J. Geophys. Res. 89, 8339–8369.
- Holycross, M.E., Watson, E.B., 2016. Diffusive fractionation of trace elements in basaltic melt. Contrib. Mineral. Petrol. 171, 80.
- Holycross, M.E., Watson, E.B., Richter, F.M., Villeneuve, J., 2018. Diffusive fractionation of Li isotopes in wet, highly silicic melts. Geochem. Perspect. Lett. 6, 39–42.
- Hu, Y., Teng, F.Z., Chauvel, C., 2021. Potassium isotopic evidence for sedimentary input to the mantle source of Lesser Antilles lavas. Geochim. Cosmochim. Acta 295, 98–111.
- Hui, H., Zhang, Y., Xu, Z., Behrens, H., 2008. Pressure dependence of the speciation of dissolved water in rhyolitic melts. Geochim. Cosmochim. Acta 72, 3229–3240.
- Jackson, M.G., Weis, D., Huang, S., 2012. Major element variations in Hawaiian shield lavas: source features and perspectives from global ocean island basalt (OIB) systematics. Geochem. Geophys. Geosyst. 13, Q09009.
- Jambon, A., 1980. Isotopic fractionation: a kinetic model for crystals growing from magmatic melts. Geochim. Cosmochim. Acta 44, 1373–1380.
- Lunar Sample Prelliminary Examination Team, 1969. Preliminary examination of lunar samples from Apollo 11: a physical, chemical, mineralogical, and biological analysis of 22 kilograms of lunar rocks and fines. Science 165, 1211–1227.
- McDonough, W.F., Sun, S.-S., Ringwood, A.E., Jagoutz, E., Hofmann, A.W., 1992. Potassium, rubidium, and cesium in the Earth and Moon and the evolution of the mantle of the Earth. Geochim. Cosmochim. Acta 56, 1001–1012.
- Neuman, M., Holzheid, A., Lodders, K., Fegley Jr., B., Jolliff, B.L., Koefoed, P., Chen, H., Wang, K., 2022. High temperature evaporation and isotopic fractionation of K and Cu. Geochim. Cosmochim. Acta 316, 1–20.
- Renne, P.R., Deino, A., Hilgen, F.J., Kuiper, K.F., Mark, D.F., Mitchell, W.S., Morgan, L.E., Mundil, R., Smit, J., 2013. Time scales of critical events around the Cretaceous-Paleogene boundary. Science 339, 684–687.
- Richter, F.M., Dauphas, N., Teng, F.Z., 2009b. Non-traditional fractionation of non-traditional isotopes: evaporation, chemical diffusion and Soret diffusion. Chem. Geol. 258, 92–103.
- Richter, F.M., Davis, A.M., DePaolo, D.J., Watson, E.B., 2003. Isotope fractionation by chemical diffusion between molten basalt and rhyolite. Geochim. Cosmochim. Acta 67, 3905–3923.
- Richter, F.M., Liang, Y., Davis, A.M., 1999. Isotope fractionation by diffusion in molten oxides. Geochim. Cosmochim. Acta 63, 2853–2861.
- Richter, F.M., Watson, E.B., Chaussidon, M., Mendybaev, R., Christensen, J.N., Qiu, L., 2014. Isotope fractionation of Li and K in silicate liquids by Soret diffusion. Geochim. Cosmochim. Acta 138, 136–145.
- Richter, F.M., Watson, E.B., Mendybaev, R.A., Dauphas, N., Georg, B., Watkins, J.M., Valley, J.W., 2009a. Isotopic fractionation of the major elements of molten basalt by chemical and thermal diffusion. Geochim. Cosmochim. Acta 73, 4250–4263.
- Richter, R.M., Watson, E.B., Mendybaev, R.A., Teng, F.Z., Janney, P.E., 2008. Magnesium isotope fractionation in silicate melts by chemical and thermal diffusion. Geochim. Cosmochim. Acta 72, 206–220.
- Sato, H., 1975. Diffusion coronas around quartz xenocrysts in andesite and basalt from Tertiary volcanic region in northeastern Shikoku, Japan. Contrib. Mineral. Petrol. 50, 49–64.
- Teng, F.Z., Dauphas, N., Watkins, J.M., 2017. Non-traditional stable isotopes: retrospective and prospective. Rev. Mineral. Geochem. 82, 1–26.
- Wang, K., Jacobsen, S.B., 2016. Potassium isotopic evidence for a high-energy giant impact origin of the moon. Nature 538, 487–490.
- Wang, Z.Z., Teng, F.Z., Prelevic, D., Liu, S.A., Zhao, Z., 2021. Potassium isotope evidence for sediment recycling into the orogenic lithospheric mantle. Geochem. Perspect. Lett. 18, 13–17.
- Watkins, J.M., DePaolo, D.J., Huber, C., Ryerson, F.J., 2009. Liquid composition-dependence of calcium isotope fractionation during diffusion in molten silicates. Geochim. Cosmochim. Acta 73, 7341–7359.
- Watkins, J.M., DePaolo, D.J., Ryerson, F.J., Peterson, B.T., 2011. Influence of liquid structure on diffusive isotope separation in molten silicates and aqueous solutions. Geochim. Cosmochim. Acta 75, 3103–3118.
- Watkins, J.M., DePaolo, D.J., Watson, E.B., 2017. Kinetic fractionation of non-traditional stable isotopes by diffusion and crystal growth reactions. Rev. Mineral. Geochem. 82, 85–125.
- Watkins, J.M., Liang, Y., Richter, F., Ryerson, F.J., DePaolo, D.J., 2014. Diffusion of multi-isotopic chemical species in molten silicates. Geochim. Cosmochim. Acta 139, 313–326.
- Watson, E.B., 1982. Basalt contamination by continental crust: some experiments and models. Contrib. Mineral. Petrol. 80, 73–87.

- Wu, H., He, Y., Teng, F.Z., Ke, S., Hou, Z., Li, S., 2018. Diffusion-driven magnesium and iron isotope fractionation at a gabbro-granite boundary. Geochim. Cosmochim. Acta 222, 671–684.
- Zhang, Y., 2008. Geochemical Kinetics. Princeton University Press, Princeton, NJ.
- Zhang, Y., 2020. H2O and other volatiles in the Moon, 50 years and on. ACS Earth Space Chem. 4.
- Zhang, Y., Gan, T., 2022. Diffusion in melts and magmas. Rev. Mineral. Geochem. 87. In press.
- Zhang, Y., Ni, H., Chen, Y., 2010. Diffusion data in silicate melts. Rev. Mineral. Geochem. 72, 311–408.
- Zhang, Y., Stolper, E.M., Wasserburg, G.J., 1991. Diffusion of a multi-species component and its role in the diffusion of water and oxygen in silicates. Earth Planet. Sci. Lett. 103, 228–240.
- Zhang, Y., Walker, D., Lesher, C.E., 1989. Diffusive crystal dissolution. Contrib. Mineral. Petrol. 102, 492–513.